The structural behavior of electrochemically delithiated $Li_xNi_{0.8}Co_{0.15}Al_{0.05}O_2$ (x<1) battery cathodes

T. Hölderle [a,b], M. Monchak [c], V. Baran [b,d], O. Dolotko [b,c], S. Bette [e], D. Mikhailova [f], A. Voss [f], M. Avdeev [g,h], H. Ehrenberg [c], P. Müller-Buschbaum [a,b], A. Senyshyn [a,b,*]

[a] *Lehrstuhl für Funktionelle Materialien, Physik Department, Technische Universität München, James-Franck Straße 1, 85748, Garching, Germany*
[b] *Heinz Maier-Leibnitz Zentrum (MLZ), Technische Universität München, Lichtenbergstraße 1, 85748, Garching, Germany*
[c] *Institute for Applied Materials (IAM), Karlsruhe Institute of Technology (KIT), 76344, Eggenstein-Leopoldshafen, Germany*
[d] *Deutsches Elektronen Synchrotron (DESY), Notkestr. 85, 22607, Hamburg, Germany*
[e] *Scientific Facility X-ray Diffraction, Max Planck Institute for Solid State Research, Heisenbergstrasse 1, Stuttgart, 70569, Germany*
[f] *Leibniz Institute for Solid State and Materials Research (IFW) Dresden e.V., D-01069, Dresden, Germany*
[g] *Australian Centre for Neutron Scattering, Australian Nuclear Science and Technology Organisation (ANSTO), New Illawarra Rd, Lucas Heights NSW 2234, Sydney, Australia*
[h] *School of Chemistry, University of Sydney, NSW, 2006, Sydney, Australia*

A B S T R A C T

A full series of variously delithiated $Li_xNi_{0.8}Co_{0.15}Al_{0.05}O_2$ (NCA) ($x < 1$) battery cathodes is extracted from cylinder Li-ion batteries of 18650-type, and structural studies of electrode materials are performed *ex situ* applying high-resolution neutron powder diffraction. A set of structural and microstructural parameters at different state-of-charges (SOC) is gathered from full-profile Rietveld refinements. Accurate cell metrics of the NCA lattice are obtained and compared for both, ex situ and operando modes of data collection. A detailed analysis of lithium occupancies and interatomic distances in the NCA cathode is carried out, revealing a shrinking material response of the NCA structure during delithiation, while the experimental quantification of Li/Ni cation mixing showed an SOC independent behavior. The observed deintercalation driven anisotropic broadening of the Bragg reflections in real-life NCA cathodes were analyzed and assigned to an increasing internal anisotropic microstrain, which is linked to the non-uniform distribution of Li in the structure of NCA, resulting in an unstable and unpredictable performance of LIBs.

1. Introduction

After the commercialization of lithium-ion batteries (LIB) by Sony in 1991, the related developments of portable electronic devices, from laptops and headphones up to today's modern smartphones, experienced an increasing popularity and progress [1,2]. Nevertheless, the growing demand on batteries and the development of new applications, like electrified drivetrains, as well as large-scale energy storage, constantly enquire for LIBs with higher energy and power densities, improved cycling life, better performance and safety, and all this at lower costs [1,3,4]. Most of the above-mentioned demands can be directly related to the materials utilized in Li-ion batteries and the development of LIBs can be vis-à-vis associated with the progress of battery cathodes. The $LiCoO_2$ cathode material utilized in the first patented LIB was proposed by J. Goodenough in 1980 [5–7] as a next generation follower of very successful $LiTiS_2$ [8,9]. Positive electrodes based on $LiCoO_2$ have a very successful history. They display high energy density, good cycling reversibility and structural stability, supplying their active use over the years. However, the high reactivity of CoO_2 along with the high cost, limited availability and localized abundance of

* Corresponding author. Lehrstuhl für Funktionelle Materialien, Physik Department, Technische Universität München, James-Franck Straße 1, 85748, Garching, Germany.
E-mail address: anatoliy.senyshyn@gmail.com (A. Senyshyn).

cobalt metal, stimulated the search for alternative cathode materials. The complete substitution of cobalt by nickel resulting in $LiNiO_2$ (LNO) is considered as a viable alternative [10,11]. However, the material suffers from poor thermal stability along with rapid capacity and power density fading. Furthermore, the introduction of nickel to the Li containing cathode is often supplemented by the formation of antisite defects (cation mixing), where nickel tends to change its oxidation state from Ni^{3+} to Ni^{2+}, thus getting even more similar in its ionic radii to Li^{+} [12–14], which, in turn, results in the partial occupational exchange of the lithium octahedral site by nickel and *vice versa*. The resulting structural disorder is considered as a negative factor, e.g. in the form of the limitation in diffusivity of lithium, due to the blocking of the 2D diffusion pathways of Li^{+} by Ni^{2+} during cycling, leading to the reduction of the cell capacity and to decreased structural stability.

Nevertheless, several families of ternary transition metal (TM) mixed oxides, either nickel-manganese or nickel-aluminum doped $LiCoO_2$, got their use in state-of-the-art LIBs. In such a way, doped $LiCoO_2$ materials typically display higher energy and power density at lower costs. They can withstand higher cycling rates and are essentially safer than the $LiCoO_2$ parent compound. Among various dopants, nickel remains highly advantageous. However, maintaining the structural integrity in high nickel content cathodes requires a low scale incorporation of either aluminum or manganese [15,16]. The Li/Ni cation mixing is an important parameter to determine the overall cell performance and lifetime in such systems. Nevertheless, the increase of nickel content in NMC materials is one of the most straightforward and viable approaches to increase the performance of LIBs, maintaining the overall chemistry of the cathode quasi unchanged.

In the current work, we are considering a high nickel content $LiNi_{0.8}Co_{0.15}Al_{0.05}O_2$ (NCA) cathode material [17,18]. Similar to $LiCoO_2$, it crystallizes in a rhombohedral structure with space group *R-3m* in a triple block ABCABC stacking sequence built up by alternating blocks of lithium ions and transition-metal ions of trivalent coordination sitting on the octahedral positions, each separated by a layer of oxygen atoms (Li_xTMO_2 block) [19–21]. The material got broad use as a positive electrode in high energy cells, which are characterized by stable and predictable cycling behavior, high energy densities etc. For instance, NCA-based full cells are actively used in the automotive industry, e.g. the 18650-type was utilized as an energy storage solution in Tesla Model S of the first generation [22,23]. However, besides its relative popularity, the accurate and systematic investigations of its structure and its coupling to the battery performance are rather limited, e.g. an increasing structural disorder at higher SOCs was reported along the c axis, resulting in the fading of the battery performance [24–26]. Additionally, antisite types of disorder for $LiNiO_2$ and a series of $Li(Ni_xMn_yCo_z)O_2$ (x + y + z = 1) (NMC) structures are broadly discussed in literature [27,28]. Theoretical simulations of physical and chemical behavior of antisite defects by either using force-field [29–31] or density functional theory [32] were reported. Additionally, experimental studies using electron diffraction revealed a controlled ordering of Li/Ni vacancies on the tetrahedral site of the Li slab [33]. A dependence between the NMC composition and the antisite defect concentration was established by using combined X-ray and neutron diffraction studies [34]. Two techniques are generally utilized for the quantification of Li \Ni cation mixing, as following.

(i) Analysis of intensity ratio for 003/104 Bragg reflections couple [35,36].
(ii) Full-profile Rietveld analysis including simulation of Li\Ni mixed occupancies [37].

It is worth to be noted that most of the studies focus on the characterization of cation mixing in synthetic NMC-based cathodes [38–41], while the presence and the effect of cation mixing in the NCA-type materials and their real-life behavior have been little explored.

In order to address this topic in a systematic and non-ambiguous way, *ex situ* and *operando* neutron powder diffraction studies on differently electrochemically delithiated NCA cathode materials, harvested from commercial 18650-type batteries is presented in a broad range of compositions. The focus is set on the structural behavior of the NCA cathode, where structural parameters are obtained by full-profile Rietveld refinement using high-resolution neutron diffraction data directly correlated to the electrochemical data.

2. Experimental

A set of fresh commercial cylindrical lithium-ion batteries of type 18650 (Panasonic NCR18650B) based on NCA|C chemistry was chosen for the studies. Their nominal capacity was 3360 mAh with an operational voltage window of 2.5–4.2 V, corresponding to a gravimetric energy density of around 240 Wh kg^{-1} as well as a volumetric energy density of around 670 Wh L^{-1} [42,43]. The cells taken from the same batch were galvanostatically cycled several times in the 2.5–4.2 V potential window using constant-current constant-voltage (CCCV) by applying ~ C/8 (0.4 A) current and C/20 cut-off current. The cycling was executed with a VMP3 potentiostat from BioLogic and ended in a fully discharged state. Afterwards, the cells were charged to a specific state of charge (SOC) with the same parameters. Below SOC 90%, the constant current charging mode was applied, whilst to achieve higher SOCs a CV stabilization was used. In total, a set of 26 cells with different stabilized SOC was prepared. However, the applied charging protocol was not able to retain the full capacity of the cell, leaving a fully charged state of 3307mAh, corresponding to ca. 98% of the nominal capacity. Therefore, in the following contribution, the charge state of 3307 mAh is referred to as fully charged state and mentioned as 100%. The cells were disassembled in the glove box from MBraun under an argon atmosphere having a humidity and O_2 level below 1 ppm. Electrode sheets were taken apart and rolled separately. The separated NCA cathode rollovers were placed into thin wall vanadium containers (150-μm wall thickness and ca. 10 mm in diameter) and metal sealed under argon for further neutron studies.

The high-resolution neutron powder diffraction measurements were carried out in Debye-Scherrer geometry at the powder diffractometers SPODI [44–46] (FRM II, Garching b. München, Germany) and ECHIDNA [47] (ANSTO, Sydney, Australia). The used experimental setup was similar in both cases. At SPODI the higher monochromator take-off angle of 155° and the 551 reflection of the vertical focusing germanium monochromator supplied a monochromatic neutron beam with a wavelength λ = 1.5482 Å. The incident beam in front of the sample has a dimension of 20 × 40 mm (h x v). The angular dependence of the scattered neutron intensities was collected with a vertically sensitive curved multidetector covering an angular range of 160° and consisting out of 80 ^{3}He detector tubes with 10' Soller collimators in front of each. The vanadium containers were mounted at a sample changer on the diffractometer table having 10 positions. The typical data acquisition time per pattern was in the range of hours. Measurements of a $Na_2Ca_3Al_2F_{14}$ filled vanadium container served as a reference for instrumental contributions to peak broadening. Examples of selected data from SPODI and ECHIDNA for selected SOCs are presented in Figs. S1 and S2, accordingly.

Additionally, *operando* measurements were carried out at SPODI on an activated fresh commercial lithium-ion battery of type 18650 (Panasonic NCR18650B) with an experimental setup different from this mentioned above. The monochromator take-off angle of 155° and the 331 reflection of the vertically focusing germanium monochromator maintained monochromatic neutrons with a wavelength of λ = 2.536 Å and a beam dimension of 20 × 40 mm^2 (h x v) in front of the sample. The cell was firmly mounted to the sample table and connected to a BioLogic VMP3 potentiostat, maintaining a slow cycle program with a charging/discharging rate of ~C/44 (75mAh) and cycling limits of 2.5V lower and 4.2V upper voltage cut-off. The collected *in operando* data (Fig. S3) was acquired with a time discretization of 30 min per pattern, corresponding

to an acquisition time of 45s, including the stepwise positioning of the multidetector (40 steps) to cover the entire diffraction angle of 160°.

The obtained 2D diffraction data were reduced to 1D diffraction patterns using a geometrical data correction. The reduced neutron diffraction data were modeled using full-profile Rietveld method as implemented in the FullProf program package [48,49], where each diffraction pattern was analyzed separately. The peak profile shape was described by the Thompson-Cox-Hastings pseudo-Voigt function and a linear interpolation between a set of manually selected background points was used to model the background.

In order to verify the modeled data by the Rietveld method, various chemical reference measurements were carried out via an inductively coupled plasma optical emission spectroscopy (ICP-OES) method to determine the elemental composition of the cathode material $Li_xNi_{0.8}Co_{0.15}Al_{0.05}O_2$ ($x < 1$) quantitatively and with high precision, representing the state of charge of the cell [50]. For this contribution, portions of the NCA material of 30 or 50 mg from the disassembled cells were scrubbed off, collected from the current collector, and dissolved in a solution containing 3 ml HCl (37% p. a., Fa. Merck) and 1 ml HNO_3 (65% p. a., Fa. Merck) in a microwave equipment (Fa. CEM) during 15 min at 180 °C. After dissolving, the solution was diluted to 500 or 1000 g and utilized for further analyses, which have been performed using an ICP-OES system (iCAP 6500 Duo View, Fa. Thermo Fisher Scientific) at the IFW Dresden.

3. Results and discussion

The obtained diffraction data exhibit the contribution from two phases corresponding to the signal from the layered NCA cathode material and the diffraction from the aluminum foil, which corresponds to the current collector. Note that the electrode material was not scraped from the current collector, but the electrode sheet was re-rolled new and contained in the sealed vanadium tubes. The layered transition metal oxide $Li_xNi_{0.8}Co_{0.15}Al_{0.05}O_2$ shows a single-phase behavior during the electrochemical cycle. It crystallizes in a $NaCrS_2$ type structure with the space group R-3m corresponding to a rhombohedral unit cell depicted in Fig. 1. Structural parameters of NCA were chosen from Ref. [51] as a starting model for full-profile Rietveld refinements of the obtained *ex situ* neutron diffraction data.

The scale factor, angular shift, cell parameters, asymmetric parameters, displacement parameters, as well as microstructural parameters in the form of anisotropic strain and size parameters were refined during the data analysis. The only atomic coordinate to be refined was the oxygen z/c fractional coordinate on the 6c site (0,0,z). The best results in terms of fit convergence were obtained for the model, where the displacement parameter at the 3a site was fixed to 1.7 Å supplying stability of the fit. Considering only an exchange of the nickel and lithium ions, due to their similar radii in terms of cation mixing [52], the occupancies of lithium and nickel distributed over the 3a (0,0,0) and 3b (0,0,1/2) site is described in more detail below. Fixed isotropic displacement parameters at the 3a site enabled the obtaining of realistic lithium concentrations and calculation of atomic occupancies at 3a and 3b sites in the structure (see section 3.2).

An example of the collected diffraction data corresponding to a discharged (SOC = 0.0%) and charged (SOC = 100.0%) state, along with the results of their simulations using the full-profile Rietveld method is shown in Fig. S1. The patterns contain the diffraction signatures of the NCA phase combined with the aluminum phase of the current collector. The diffraction signal from the current collector remains unchanged vs. SOC, while in the NCA phase, a systematic shift of the Bragg reflections, as well as a change of widths for selected peak families, was observed as a response on the delithiation of the material supplementing the increase of SOC. The best fits were obtained with the structural parameters for the cathodes listed in Table 1. Graphical representations of Rietveld fit quality for the data collected for a charged state (SOC = 100.0%) at two distinct wavelengths at the instrument ECHIDNA (ANSTO) is presented in Fig. S2.

3.1. Lattice parameter analysis

Facing higher charging states results in the reduction of the Li content, leading to a systematic structural distortion, which in turn, reflects in the shifts of Bragg reflections. In Fig. 2, a couple of characteristic reflections 003 and 104 are shown, representing the structural evolution of the NCA material along *c*- and *a*-direction, respectively. At the beginning, the 003 reflection displays a shift towards lower 2θ angles, reaches the "minimum" around SOC≈75% and then "relaxes" back, which can be directly linked to a change of the unit cell dimension along the *c*-axis (Fig. 1(c)). At the initial stage of lithium extraction, the *c* lattice parameter increases linearly from 14.21697 Å by 0.27312 Å corresponding to ca. 1.9% linear elongation, which is attributed to the electrostatic binding energy of lithium ions in the NCA structure maintaining the integrity of TMO_2 layers (TM – transition metal), as well as the oxidation of Ni and Co to tetravalent states. When lithium ions are extracted, the TMO_2 layers exhibit an increase in electrostatic repulsion due to the increasing interactions between negatively charged oxygen-oxygen layers resulting in an elongation of the unit cell in *c*-direction until a maximum expansion at a lithium content of ca. $Li_x \approx 0.3$ is reached [53–55]. Upon further delithiation, the lattice in the *c*-direction rapidly contracts at the vicinity of critical lithium occupancy at $Li_x \approx 0.3$ by 0.31291 Å corresponding to ca. 2.2%. Accordingly, the structure undergoes an increase in the valence charge of transition metals (for

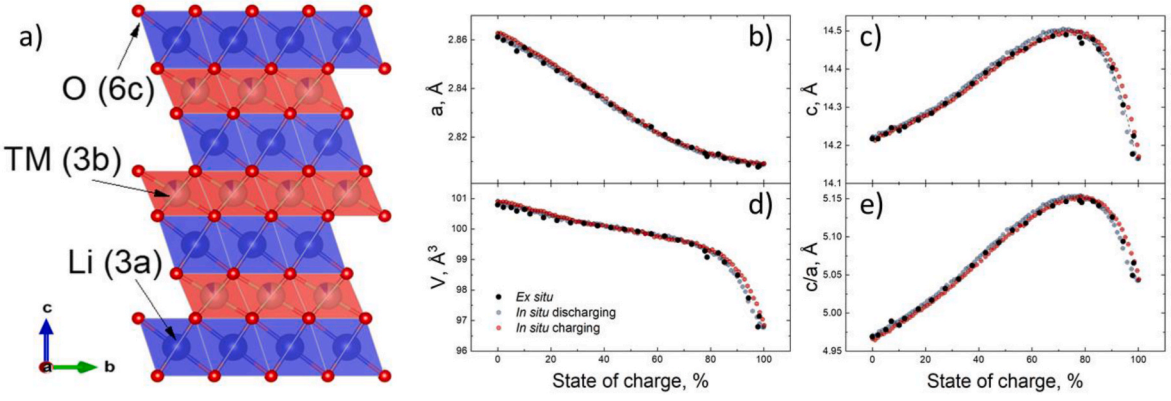

Fig. 1. Structure of NCA cathode (a), change of lattice metrics in a- and c-direction of rhombohedral lattice (b, c), lattice volume (d) and c/a ratio (e). *Ex situ* data are presented by black points, whilst *in operando* data are marked by red color while charging and in blue while discharging. Solid lines in a- and c-lattice parameters correspond to 6th order polynomial fitting the experimental cell dimensions with coefficients listed in Table S2. (For interpretation of the references to color in this figure legend, the reader is referred to the Web version of this article.)

Table 1
Structural parameters of $Li_xNi_{0.8}Co_{0.15}Al_{0.05}O_2$ cathode material (spacegroup *R-3m*, no.166) harvested from NCA 18650-type commercial lithium-ion batteries.

SOC [%]	Q [mAh]	Li_x [f. u.]	Lattice Parameter			Li site occupancy		B-factor		Oxygen coordinate	Reliability factors [f. u.]		
			a [Å]	*c* [Å]	*c/a*	3a [f. u.]	3b [f. u.]	Li1 [Å]	Li2 [Å]	6a z/c [f. u.]	R_p	R_{wp}	X^2
0	0	0.89860	2.86116(1)	14.21697(7)	4.9690(2)	0.074(2)	0.0003(3)	1.7	0.12(1)	0.2396(3)	6.71	5.74	3.13
2.1	71	0.90028	2.85992(1)	14.21719(6)	4.9712(2)	0.075(2)	0.0003(2)	1.7	0.15(1)	0.2396(3)	6.50	5.31	2.03
5.1	170	0.84327	2.85854(1)	14.23015(7)	4.9781(2)	0.070(2)	0.0005(3)	1.7	0.15(1)	0.2393(3)	6.97	6.00	3.46
7.2	241	0.73611	2.85535(1)	14.24558(7)	4.9891(2)	0.061(2)	0.0001(3)	1.7	0.22(1)	0.2388(4)	7.02	5.99	3.34
10.1	340	0.79443	2.85684(1)	14.23836(6)	4.9840(2)	0.066(2)	0.0003(3)	1.7	0.20(1)	0.2390(3)	6.48	5.28	2.42
12.2	411	0.76683	2.85377(1)	14.24821(6)	4.9928(2)	0.063(2)	0.0002(3)	1.7	0.20(1)	0.2386(3)	6.65	5.42	2.55
17.3	581	0.73911	2.85032(1)	14.26615(7)	5.0051(2)	0.061(2)	0.0001(3)	1.7	0.16(1)	0.2382(3)	6.54	5.45	2.64
22.3	751	0.65079	2.84724(1)	14.28385(7)	5.0167(2)	0.054(2)	0.0008(3)	1.7	0.18(1)	0.2378(4)	6.51	5.62	3.11
27.4	921	0.63675	2.84361(1)	14.30927(8)	5.0321(2)	0.053(2)	0.0003(3)	1.7	0.22(1)	0.2374(4)	6.83	5.78	3.10
32.4	1091	0.52934	2.84101(2)	14.3321(2)	5.0447(3)	0.044(3)	0.0009(4)	1.7	0.30(2)	0.2371(5)	8.80	8.12	6.20
37.5	1261	0.54842	2.83699(2)	14.3615(2)	5.0622(3)	0.045(3)	0.0001(4)	1.7	0.25(2)	0.2368(5)	8.28	7.26	4.83
42.6	1431	0.56786	2.83332(2)	14.3905(2)	5.0790(3)	0.047(3)	0.0005(4)	1.7	0.22(3)	0.2365(7)	9.10	8.27	7.28
47.6	1601	0.50090	2.83036(2)	14.4128(2)	5.0922(4)	0.041(3)	0.0003(4)	1.7	0.24(3)	0.2362(7)	9.54	8.59	7.81
52.7	1771	0.45578	2.82665(1)	14.4399(2)	5.1085(3)	0.037(2)	0.0002(3)	1.7	0.32(2)	0.2358(5)	6.62	6.13	3.93
57.7	1941	0.38510	2.82417(1)	14.4534(2)	5.1178(3)	0.032(2)	0.0006(3)	1.7	0.34(2)	0.2355(5)	6.44	6.03	4.09
62.8	2111	0.40334	2.82101(2)	14.4753(2)	5.1313(3)	0.033(2)	0.0001(4)	1.7	0.31(2)	0.2351(5)	6.46	6.05	3.93
67.8	2281	0.33469	2.81814(2)	14.4859(2)	5.1402(3)	0.027(2)	0.0001(4)	1.7	0.33(2)	0.2348(5)	6.28	5.89	3.93
72.9	2451	0.30265	2.81578(2)	14.4901(2)	5.1460(4)	0.025(3)	0.0001(4)	1.7	0.33(2)	0.2345(6)	6.59	6.26	4.10
77.9	2621	0.26929	2.81343(2)	14.4828(2)	5.1477(4)	0.022(3)	0.0000(4)	1.7	0.28(2)	0.2343(5)	6.36	6.01	3.95
78.7	2648	0.18745	2.81205(2)	14.4676(2)	5.1449(4)	0.015(3)	0.0006(4)	1.7	0.35(2)	0.2341(4)	7.35	6.66	5.22
83.0	2790	0.24205	2.81304(2)	14.4776(2)	5.1466(4)	0.020(2)	0.0000(4)	1.7	0.37(2)	0.2342(4)	7.24	6.65	5.31
85.2	2864	0.18145	2.81128(2)	14.4521(2)	5.1407(4)	0.015(3)	0.0004(4)	1.7	0.37(2)	0.2341(4)	7.30	6.59	5.37
90.2	3035	0.13885	2.80994(1)	14.4028(2)	5.1257(4)	0.011(2)	0.0005(4)	1.7	0.39(2)	0.2340(4)	7.42	6.51	5.13
94.3	3171	0.13585	2.80862(1)	14.3061(2)	5.0936(3)	0.011(2)	0.0007(3)	1.7	0.26(1)	0.2344(4)	6.36	5.73	4.24
97.9	3291	0.17605	2.80810(1)	14.2244(2)	5.0665(3)	0.014(2)	0.0006(3)	1.7	0.24(1)	0.2347(4)	6.20	5.42	3.36
98.3	3307	0.18649	2.80772(1)	14.1772(2)	5.0494(3)	0.015(2)	0.0008(3)	1.7	0.24(1)	0.2347(4)	6.57	5.32	3.30

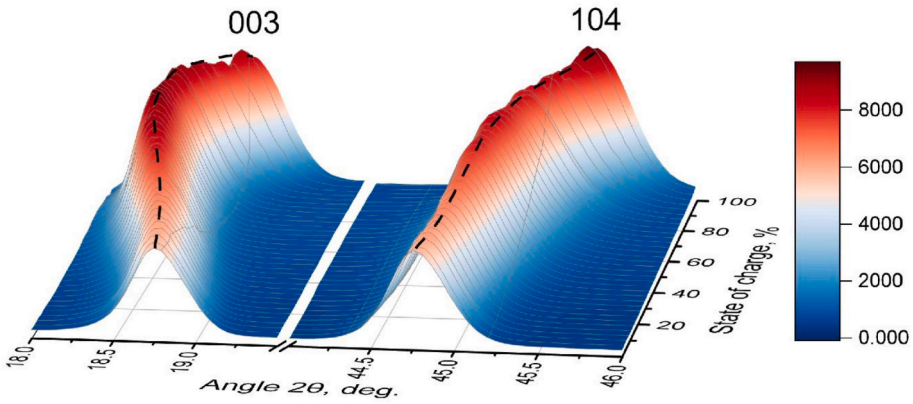

Fig. 2. Evolution of 003 and 104 reflections for NCA as a function of the state of charge. Dashed lines illustrate the shifts of Bragg reflections maxima vs. de/lithiation.

instance $Ni^{3+} \rightarrow Ni^{4+}$) at higher charged states and a simultaneous decrease of valence charge on the oxygen ions, which results in the weakening of the electrostatic repulsion between the TMO_2 layers and in a contraction of the unit cell in *c* direction. A further collapse of the structure upon charging is prevented by the electrostatic attraction between negatively charged oxygen's and the remaining positively charged Li ions (screening effect) in the structure of NCA [56]. Although, the deeper lithium extraction allows even a further shrinkage beyond the initial lengths of lattice parameter *c* [57–59].

In contrast to the 003 reflection, the position of 104 Bragg reflection is defined by both, c- and a-parameters of the rhombohedral lattice (in a hexagonal setting). Its behavior vs. SOC substantially differs from the 003 one, i.e. upon the increase of SOC, the position of the 104 reflection undergoes a shift towards higher 2θ angles in the whole range. Such behavior corresponds to a non-linear contraction of the hexagonal lattice in *a* (=*b*) direction 2.86116(1) Å at a SOC of 0%–2.80772(1) Å at a SOC of 100%, which is ca. 1.87% in terms of relative elongation. The lattice contraction in *a*-direction is non-linear, i.e. a change of slope occurs at ca. SOC≈75% ∝ $Li_x \approx 0.3$, thus separating regions with a rapid and slow decrease of a lattice parameter, see Fig. 1(b).

Considering the effect of Li content on the interatomic distances yields a totally distinct behavior/response of Li–O (3a-6c), TM-O (3b-6c) and O–O (6c-6c) interatomic distances on the delithiation. All interatomic distances are exclusively determined by three parameters, *a*- and *c*-lattice parameter and z oxygen coordinate. The TM-O bond-length in Å displays a linear decrease vs. SOC, i.e. by 3.2% relative elongation starting from 1.9507(3) (Fig. S4), whilst the behavior of Li–O distance resembles this of c-lattice parameter: a quasi-linear increase below SOC ≈75% and increased negative deviations from linear behavior at higher SOCs. The linear decrease of TM-O interatomic distances can be attributed to the oxidation of Ni^{3+} to Ni^{4+}, leading to the decrease of its ionic radius [12] and an increased covalent contribution of the Ni–O bond. The linear increase of Li–O distances vs. lithium removal may be linked with the above-mentioned complex and repulsive character of oxygen-oxygen interactions.

Therefore, oxygen-oxygen (6c-6c) distances resemble different responses defined by three different interatomic distances within the NCA structure (Fig. S4). The first "family" of oxygen-oxygen (6c-6c) interatomic distances can be found in the apicals and vertices of both, the LiO_6 and the TMO_6 octahedra (Fig. S11), describing the interatomic distances of the oxygen layer separating the Li slab from the TM slab. The second kind of interatomic oxygen-oxygen distance is found in the TMO_6 octahedral connecting their vertices and apicals. Both bond lengths show a quasi-linear decrease in their distances upon charging, which can be coupled to the evolution of the unit cell during electrochemical cycling in *a* and *b* direction. Additionally, a third group of equal oxygen-oxygen (6c-6c) interatomic distances is represented in

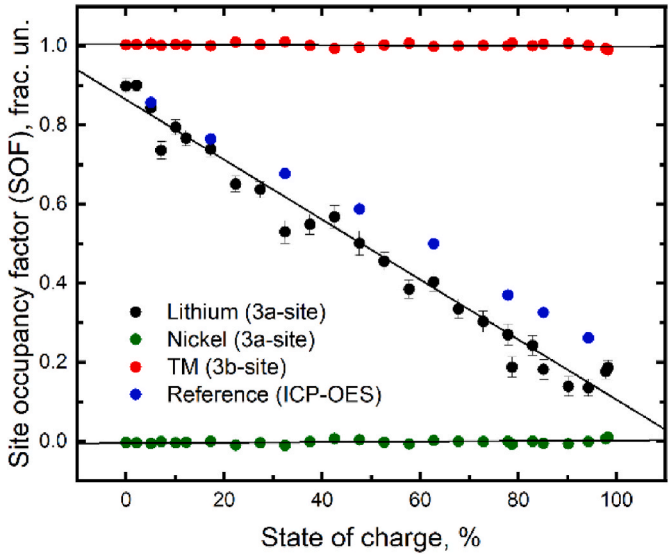

Fig. 3. Evolution of refined site occupancies in NCA-type cathode vs. applied state-of-charge. Red points correspond to transition-metal concentrations at the 3b site, the green points and black points illustrate Ni and Li at 3a, the blue points result from ICP-OES. (For interpretation of the references to color in this figure legend, the reader is referred to the Web version of this article.)

selected LiO_6 octahedral apicals and vertices, which show increasing behaviour, followed by shrinking interatomic distances, similar to the evolution of the unit cell in c direction.

The results on lattice metrics in the *operando* dataset are in good agreement with those obtained using the *ex situ* method. Large incoherent scattering cross-sections for hydrogen, nickel and cobalt along with the fact that the neutron diffraction dataset collected *operando* is dominated by the signal from the graphite anode (Fig. S5), steel housing and current collector makes the high-quality structural characterization of the cathode materials not trivial. However, the mentioned effects like the cation mixing and the systematics of the atomic displacements require a scattering contrast better than this available from non-resonant X-ray diffraction. This was the primary motivation for carrying out *ex situ* studies and detailed modeling of the structure results.

3.2. *Lithium occupancy analysis*

In the $LiCoO_2$ battery electrode, the lithium is located exclusively at the 3a (0, 0, 0) interlayer atomic site. Nickel doping in various contents, either in the form of NCA or NCM cathodes, has been reported to exhibit

Li/Ni cation mixture leading to the appearance of lithium on the interlayer 3b (0, 0, 1/2) site [37], which in $LiCoO_2$ was exclusively occupied by transition metals. Considering it in the context of neutron scattering, the increase of SOC leads to a reduction of the negative structural amplitude at the 3a site, which is a direct consequence of the lithium extraction (or deintercalation). The refined lithium content at the 3a site has been found to be linearly proportional to the applied SOC (Fig. 3). At SOC = 0% the lithium occupancy corresponds to 90% of lithium content in the structure, where its deviation from nominal 100% is attributed to the irreversible capacity loss, caused by the cell formation. In a fully charged state at SOC = 100% the lithium content has been refined to 18.6% site occupancy. The determined lithium content has been found sufficiently lower than 50% lithium site occupancy and the structure has been found rhombohedral in the whole range of SOCs, i.e. no traces of rhombohedral-to-monoclinic phase transition have been observed (similar to this reported in Ref. [60]). Experimentally determined trends of lithium contents behavior have been independently confirmed by ICP-OES measurements (blue points in Fig. 3).

3.3. Transition metal occupancy analysis

Analyzing the occupancy at the transition metal (3b) site, the previously reported model of antisite disorder in NMC type materials was considered [37,61–63]. Cobalt and aluminum were assumed to be localized at the 3b site, where their occupancies were fixed to G(Co) = $\frac{3}{36}$*0.15 and G(Al) = $\frac{3}{36}$*0.05 rel. un. The total occupancy for lithium and nickel was set to $G_{total}(Li) = \frac{3}{36}$ and $G_{total}(Ni) = \frac{3}{36}$*0.8. Elemental distribution at the 3a (Li1/Ni1) and 3b (Li2/Ni2) site was refined by assuming that G(Ni1) = G(Li2) and G(Ni1) + G(Ni2) = G_{total}(Ni) [63]. The Ni obtained in this way residing at the 3a site has been found close to zero, indicating the absence of measurable Ni^{3+} migration from the 3b towards the 3a site within the sensitivity of the method. This enables us to conclude that there are no antisite defects (cation mixing) present in the structure of the NCA cathode material during the applied electrochemical cycle. Applying the volume averaged method, we cannot entirely exclude its presence on a local level, similar to this previously reported by local probe TEM [64]. Another popular way to quantify the cation mixing is the analysis of 003 and 104 Bragg reflection intensity ratio [35,36]. For example in Ref. [65] the occurrence of cation mixing has been detected and quantified in this way. Note that such evaluation is somewhat ambiguous and need to be carried out with a lot of care, e.g. taking into account that the intensity ratio of 003 and 104 reflections depend not only on Li/Ni ratio at 3a site, but also on the lithium content (Fig. S10).

In general, the lack of cation mixing in NCA-type material can be explained by the suppression of superexchange interactions between the transition metals [66–68] and their coupling to the intrinsic behavior of the post-transition metal aluminum. For instance, Ni/Li cation mixing in NMC structures happens not only due to the similar radii of Ni and Li but also due to the tendency of Ni to form strong σ bonds between the p orbital of oxygen and the e_g orbital of the nickel ion, resulting in a super exchange $Ni_{3b\text{-}site}/Mn_{3b\text{-}site}$ – O – $Ni_{3a\text{-}site}$ interlayer chain. With increasing amounts of non-magnetic low-spin Co^{3+}, the superexchange of Ni^{2+} and O^{2-} can be shielded and intermixing of Li and Ni is prevented due to the lack of unpaired electrons in its electronic structure. Materials similar to Co^{3+} without unpaired spins, such as aluminum will have the same effect on the structure [27]. The following substitution of the Mn^{4+} cation with Al^{3+} will result in the cathode structure NCA and in an even higher energy barrier for antisite defects to occur, as seen in Ref. [32]. In conclusion, the combination of cobalt and aluminum in the NCA structure may increase the energy barrier to such an extent that no more intermixing of nickel and lithium ions is further possible.

3.4. Peak broadening analysis

The evaluation of the diffraction line profiles for the studied NCA type materials reveals their systematic broadening upon increased SOC. The broadening has an anisotropic character, proceeding in certain reciprocal space directions more pronounced than in others. In the *operando* dataset, the strong peak overlap for Bragg signals from cathode and anode was observed, which is not the case for datasets collected *ex situ*. The anisotropic strain was modeled using the full-profile Rietveld method, applying the Stephens model [69]. In accordance with *-3m1* Laue class embedding the space group *R-3m* a set of three independent anisotropic strain parameters (S_{400}, S_{112}, S_{004}) and a Lorentzian strain mixing coefficient were refined.

Compared to SOC = 0%, a number of peak groups that display systematically higher reflection broadening can be observed upon delithiation. In a series of such groups, the peak FWHM is rapidly increasing with the growth of the l index, where the reflection groups 00*l* and 10*l* is most remarkable. All this indicates a highly anisotropic character of the microstrain in real battery electrodes. Note that a certain degree of anisotropy occurs already at SOC = 0%, as illustrated by the Williamson-Hall plots presented in Fig. 4a and S7. At SOC = 0%, the microstrain tensor can be represented by an ellipse, created from a sphere elongated in *c*-direction. Upon increase of the SOC, the elongated sphere continuously diverges into a two-ball shaped tensor surface with a smaller waist forming a dumbbell at SOC ≈100%.

The observed dominance of the microstrains for the l-type indexes can be attributed to the structural imperfections in a-b plane of the hexagonal lattice. Based on the structural motives of the $NaCrS_2$ lattice and excluding cation mixing, one can identify two possible sources of structural deviations in the lateral plane.

- growth of in – plane structural imperfections, leading to a loss of periodicity;
- deintercalation-induced changes in the stacking character.

The stacking aspect is broadly discussed in the literature [70] for various material classes. After many pioneering works [71–75], a

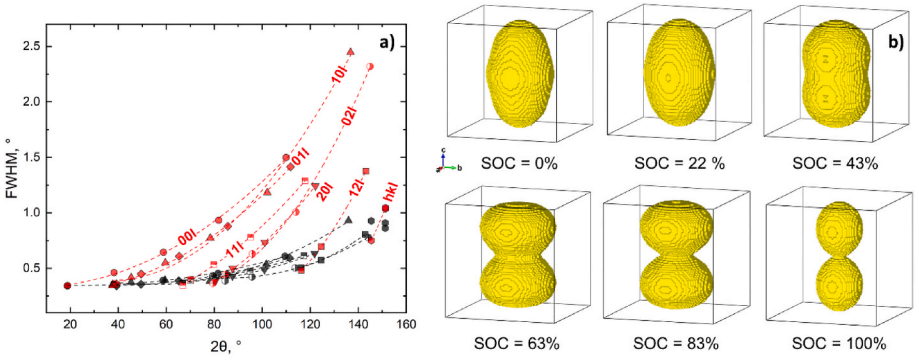

Fig. 4. (a) Angular evolution of diffraction peaks in NCA at SOC 0% (black) and 100% (red). Lines illustrate the peak families and are guides for the eyes. (right) Graphical representation of microstrain tensor at selected SOCs†.
† For animated version of the full dataset, please refer to Supplementary Information. (For interpretation of the references to color in this figure legend, the reader is referred to the Web version of this article.)

stochastic approach of modeling stacking disorder for the description of stacking systematics was realized in the program FAULTS [76,77]. This approach used the structure-relevant $LiNiO_2$ example as an illustration and was successfully applied for the modeling of stacking faults in a long series of LIB relevant materials incl. NMC and NCA [26,78–85]. Recently, a grid search optimization routine for the determination of the microstructure was developed and validated for purposefully stacking-faulted NCA [86]. The method enables the evaluation of stacking probabilities for a given defect model in a rigorous and statistically viable way. The data analysis was adapted to the neutron experiment and carried out for three representative neutron datasets, taken at SOC = 0%, ~50% and 100%. Besides the simple structure model, three possible defect configurations were evaluated, namely (see Fig. S8 for details) situations when all or just 50% of Li/NiO_6 octahedra were face sharing, as well as lithium in a tetrahedral configuration. For all three models, including faults yield only minimal improvement of R_{wp} at very low fault probabilities (Fig. S9), indicating a non-significant contribution from stacking faults. As already stated in Ref. [86], the violation of the ABC stacking order is typically reflected in the broadening of hk0 – type reflections, whilst the broadening of 00l was attributed to interstratification faults – a random intercalation of ions and molecules between the layers.

Observed increasing magnitude and anisotropy of microstrains in the NCA material can be directly associated with the formation of intragranular cracks, which may show the number of negative effects on the cell performance [87]. Crack formation and their effects on the cell operation are actively discussed in literature [88]. Their origin are often attributed to volume change and microstrains of the anisotropic lattice, e.g. due to evolving strains between primary grains during electrochemical cycling [89]. Besides this, lattice gliding [90], nanopores [91] and/or dislocation based crack incubation/spread as well as high voltage cycling [92] lead to intragranular cracking of primary grains [88]. Experimentally observed increase of microstrains in the delithiated NCA structure, along with the increase of its anisotropy, can be attributed to the heterogeneous cathode lithiation. The degree of heterogeneity increases with increase of SOC (upon cathode delithiation). Big majority of cylinder-type lithium-ion batteries are heterogeneous in nature [93,94] and their extended operation causes further stabilization and growth of a heterogeneous state [95–97]. Heterogeneities occur on different scales and in different directions [94], i.e. along and across the electrode stripes, between and within the particle grains as a consequence of the current distribution, electrolyte wetting, ionic opacity of the separator, availability of lithium *etc*. A non-uniform distribution of lithium exhibits stress on the NCA material, which develops an increasing internal strain of the structure and may lead to an unstable and unpredictable performance of the LIB.

4. Conclusion

A set of $Li_xNi_{0.8}Co_{0.15}Al_{0.05}O_2$ cathodes harvested from commercial Li-ion batteries of 18650-type were investigated using different methods. Studies were performed at predefined SOCs at which the battery was taken apart and the material was extracted for analysis. A good agreement of the structural properties with the experimental data collected *operando* is explicitly mentioned.

The analyzed NCA structure remained in a single-phase state (space group: *R-3m*) for the whole range of SOCs. The lattice parameters reflect the changes of the lithium content and the ionic radii of the transition metals upon oxidation in the NCA structure in a non-linear manner. At a characteristic lithium content corresponding to $Li_x \approx 0.25–0.30$, a remarkable slope change occurs in the unit cell in the *c*-direction affecting the Li–O and certain O–O interatomic distances. The lithium concentration has been found to be proportional to the SOC and is in good agreement with the chemical analysis of the reference NCA material conducted by ICP-OES. The analysis of mixed occupancies at both Li and TM sites revealed no detectable hints for antisite defects (cation mixing) in the structure of $Li_xNi_{0.8}Co_{0.15}Al_{0.05}O_2$ during the deintercalation/intercalation process, which is in line with its excellent cycling performance at moderate C-rates.

Besides this, the characteristic and systematic peak broadening was observed in the studied NCA materials, where the character and magnitude of the broadening depend on the SOC. The peak broadening displays an anisotropic character and was attributed to anisotropic microstrains that evolved upon delithiation. The microstrains were associated with the heterogeneous character of the lithium deintercalation in the NCA cathode. From the performed studies, however, it remains unclear whether the NCA cathode heterogeneities have a local character or represent directional gradients similar to the lithiated graphite. It will require series of additional studies with higher spatial resolution to address such questions.

CRediT authorship contribution statement

T. Hölderle: Data curation, Formal analysis, Visualization, Writing – original draft. **M. Monchak:** Methodology, Investigation. **V. Baran:** Investigation. **O. Dolotko:** Investigation. **S. Bette:** Formal analysis, Visualization. **D. Mikhailova:** Formal analysis. **A. Voss:** Formal anal-ysis, Investigation. **M. Avdeev:** Resources, Methodology. **H. Ehrenberg:** Resources, Methodology, Funding acquisition, Writing – review & editing. **P. Müller-Buschbaum:** Funding acquisition, Writing – review & editing. **A. Senyshyn:** Writing – review & editing, Project adminis-tration, Methodology.

Declaration of competing interest

The authors declare that they have no known competing financial interests or personal relationships that could have appeared to influence the work reported in this paper.

Data availability

Data will be made available on request.

Acknowledgments

The authors gratefully acknowledge the financial support provided by the Heinz Maier-Leibnitz Zentrum (Technische Universität München), German Federal Ministry of Education and Research (BMBF project 05K16VK2 and 05K19VK3) and German Research Foundation (DFG, projects EH 183/15-1, SE 2376/1-1]). This work contributes to the research performed at CELEST (Center for Electrochemical Energy Storage Ulm-Karlsruhe). Authors thank the Heinz Maier-Leibnitz Zentrum for the provision of beamtime and access to their infrastructure.

References

[1] Y. Nishi, The development of lithium ion secondary batteries, Chem. Rec. 1 (5) (2001) 406–413.
[2] X. Zuo, et al., Silicon based lithium-ion battery anodes: a chronicle perspective review, Nano Energy 31 (2017) 113–143.
[3] J.M. Tarascon, M. Armand, Issues and challenges facing rechargeable lithium batteries, Nature 414 (6861) (2001) 359–367.
[4] M. Armand, J.M. Tarascon, Building better batteries, Nature 451 (7179) (2008) 652–657.
[5] K. Mizushima, et al., Lixcoo2 "(Oless-Thanxless-Than-or-Equal-To1) - a new cathode material for batteries of high-energy density, Mater. Res. Bull. 15 (6) (1980) 783–789.
[6] J.B. Goodenough, K. Mizushima, T. Takeda, Solid-solution oxides for storage-battery electrodes, Jpn. J. Appl. Phys. 19 (S3) (1980) 305.

[7] T. Ohzuku, A. Ueda, Solid-state redox reactions of LiCoO2 (R3m) for 4 volt secondary lithium cells, J. Electrochem. Soc. 141 (11) (1994) 2972–2977.
[8] M.S. Whittingham, F.R. Gamble, The lithium intercalates of the transition metal dichalcogenides, Mater. Res. Bull. 10 (5) (1975) 363–371.
[9] M.S. Whittingham, Lithium titanium disulfide cathodes, Nat. Energy 6 (2) (2021) 214, 214.
[10] J.R. Dahn, U. von Sacken, C.A. Michal, Structure and electrochemistry of Li1 ±yNiO2 and a new Li2NiO2 phase with the Ni (OH)2 structure, Solid State Ionics 44 (1) (1990) 87–97.
[11] C. Delmas, et al., An overview of the Li(Ni,M)O2 systems: syntheses, structures and properties, Electrochim. Acta 45 (1) (1999) 243–253.
[12] R. Shannon, Revised effective ionic radii and systematic studies of interatomic distances in halides and chalcogenides, Acta Crystallogr. A 32 (5) (1976) 751–767.
[13] A. Rougier, et al., Effect of cobalt substitution on cationic distribution in LiNi1 y CoyO2 electrode materials, Solid State Ionics 90 (1) (1996) 83–90.
[14] A. Rougier, P. Gravereau, C. Delmas, Optimization of the composition of the Li1 z Ni1 + z O 2 electrode materials: structural, magnetic, and electrochemical studies, J. Electrochem. Soc. 143 (4) (1996) 1168.
[15] A. Purwanto, et al., NCA cathode material: synthesis methods and performance enhancement efforts, Mater. Res. Express 5 (12) (2018).
[16] Mineral commodity summaries 2021, in: Mineral Commodity Summaries, VA, Reston, 2021, p. 200.
[17] C.H. Chen, et al., Aluminum-doped lithium nickel cobalt oxide electrodes for high-power lithium-ion batteries, J. Power Sources 128 (2) (2004) 278–285.
[18] S. Castro-García, et al., Influence of aluminum doping on the properties of LiCoO2 and LiNi0.5Co0.5O2 oxides, Solid State Ionics 156 (1) (2003) 15–26.
[19] C. Delmas, C. Fouassier, P. Hagenmuller, Structural classification and properties of the layered oxides, Physica B C 99 (1–4) (1980) 81–85.
[20] H.D. Liu, et al., Identifying the chemical and structural irreversibility in LiNi0.8Co0.15Al0.05O2 - a model compound for classical layered intercalation, J. Mater. Chem.A 6 (9) (2018) 4189–4198.
[21] M.S. Whittingham, Lithium batteries and cathode materials, Chem. Rev. 104 (10) (2004) 4271–4302.
[22] C. Martin, Driving change in the battery industry, Nat. Nanotechnol. 9 (5) (2014) 327–328.
[23] D. Coffin, J. Horowitz, The supply chain for electric vehicle batteries, J. Int'l Com. & Econ. (2018) 1.
[24] C. Xu, et al., Phase behavior during electrochemical cycling of Ni-rich cathode materials for Li-ion batteries, Adv. Energy Mater. 11 (7) (2021), 2003404.
[25] C. Delmas, et al., Electrochemical intercalation of sodium in NaxCoO2 bronzes, Solid State Ionics 3–4 (1981) 165–169.
[26] M. Bianchini, et al., There and Back Again—The Journey of LiNiO2 as a Cathode Active Material, Angewandte Chemie International Edition 58 (31) (2019) 10434–10458.
[27] J.X. Zheng, et al., Ni/Li disordering in layered transition metal oxide: electrochemical impact, origin, and control, Accounts Chem. Res. 52 (8) (2019) 2201–2209.
[28] C.M. Julien, et al., Comparative issues of cathode materials for Li-ion batteries, Inorganics 2 (1) (2014) 132–154.
[29] J. Bréger, et al., Effect of high voltage on the structure and electrochemistry of LiNi0.5Mn0.5O2: a joint experimental and theoretical study, Chem. Mater. 18 (20) (2006) 4768–4781.
[30] A. Abdellahi, et al., Understanding the effect of cation disorder on the voltage profile of lithium transition-metal oxides, Chem. Mater. 28 (15) (2016) 5373–5383.
[31] D. Zhuang, M.Z. Bazant, Theory of layered-oxide cathode degradation in Li-ion batteries by oxidation-induced cation disorder, J. Electrochem. Soc. 169 (10) (2022), 100536.
[32] K. Hoang, M. Johannes, Defect physics and chemistry in layered mixed transition metal oxide cathode materials: (Ni,Co,Mn) vs (Ni,Co,Al), Chem. Mater. 28 (5) (2016) 1325–1334.
[33] H.H. Li, et al., Changes in the cation ordering of layered O3 LixNi0.5Mn0.5O2 during electrochemical cycling to high voltages: an electron diffraction study, Chem. Mater. 19 (10) (2007) 2551–2565.
[34] L. Yin, et al., Thermodynamics of antisite defects in layered NMC cathodes: systematic insights from high-precision powder diffraction analyses, Chem. Mater. 32 (3) (2020) 1002–1010.
[35] S.-J. Sim, et al., Use of carbon coating on LiNi0.8Co0.1Mn0.1O2 cathode material for enhanced performances of lithium-ion batteries, Sci. Rep. 10 (1) (2020), 11114.
[36] T. Ohzuku, A. Ueda, M. Nagayama, Electrochemistry and structural chemistry of LiNiO2 (R3m) for 4 volt secondary lithium cells, J. Electrochem. Soc. 140 (7) (1993) 1862–1870.
[37] O. Dolotko, et al., Understanding structural changes in NMC Li-ion cells by in situ neutron diffraction, J. Power Sources 255 (2014) 197–203.
[38] J. Jacas Biendicho, et al., Contact resistance stability and cation mixing in a Vulcan-based LiNi1/3Co1/3Mn1/3O2 slurry for semi-solid flow batteries, Dalton Trans. 50 (19) (2021) 6710–6717.
[39] H. Yu, et al., Study of the lithium/nickel ions exchange in the layered LiNi0.42Mn0.42Co0.16O2 cathode material for lithium ion batteries: experimental and first-principles calculations, Energy Environ. Sci. 7 (3) (2014) 1068–1078.
[40] G. Sun, et al., The effect of cation mixing controlled by thermal treatment duration on the electrochemical stability of lithium transition-metal oxides, Phys. Chem. Chem. Phys. 19 (44) (2017) 29886–29894.
[41] X. Zhang, et al., Synthesis and characterization of LiNi1/3Mn1/3Co1/3O2 by wet-chemical method, ECS Trans. 16 (42) (2019) 11–19.
[42] M. Hagen, et al., Lithium–sulfur cells: the gap between the state-of-the-art and the requirements for high energy battery cells, Adv. Energy Mater. 5 (16) (2015), 1401986.
[43] W. Diao, C. Kulkarni, M. Pecht, Development of an informative lithium-ion battery datasheet, Energies 14 (17) (2021) 5434.
[44] M. Hoelzel, et al., High-resolution neutron powder diffractometer SPODI at research reactor FRM II, Nucl. Instrum. Methods Phys. Res. Sect. A Accel. Spectrom. Detect. Assoc. Equip. 667 (2012) 32–37.
[45] R. Gilles, et al., First test measurements at the new structure powder diffractometer (SPODI) at the FRM-II, in: Ninth European Powder Diffraction Conference, Oldenbourg Wissenschaftsverlag, 2015.
[46] M. Hoelzel, A. Senyshyn, O. Dolotko, SPODI: high resolution powder diffractometer, Journal of large-scale research facilities JLSRF 1 (2015).
[47] M. Avdeev, J.R. Hester, ECHIDNA: a decade of high-resolution neutron powder diffraction at OPAL, J. Appl. Crystallogr. 51 (6) (2018) 1597–1604.
[48] J. Rodríguez-Carvajal, FullProf, CEA/Saclay, France, 2001.
[49] J. Rodríguez-Carvajal, An Introduction to the Program FullProf, Laboratoire Leon Brillouin (CEA-CNRS), 2001.
[50] J.W. Olesik, Elemental analysis using ICP-OES and ICP/MS, Anal. Chem. 63 (1) (1991) 12A–21A.
[51] I. Bobrikov, et al., In-situ time-of-flight neutron diffraction study of the structure evolution of electrode materials in a commercial battery with LiNi0. 8Co0. 15Al0. 05O2 cathode, J. Power Sources 372 (2017) 74–81.
[52] X. Zhang, et al., Minimization of the cation mixing in Li1+x(NMC)1 xO2 as cathode material, J. Power Sources 195 (5) (2010) 1292–1301.
[53] G.G. Amatucci, J.M. Tarascon, L.C. Klein, CoO2, the end member of the Li x CoO2 solid solution, J. Electrochem. Soc. 143 (3) (1996) 1114–1123.
[54] M.G.S.R. Thomas, P.G. Bruce, J.B. Goodenough, Lithium mobility in the layered oxide Li1 xCoO2, Solid State Ionics 17 (1) (1985) 13–19.
[55] L. Pinsard-Gaudart, et al., Growth and characterisation of LixCoO2 single crystals, J. Cryst. Growth 334 (1) (2011) 165–169.
[56] L. Vegard, Die Konstitution der Mischkristalle und die Raumfüllung der Atome, Z. Phys. 5 (1) (1921) 17–26.
[57] S. Laubach, et al., Changes in the crystal and electronic structure of LiCoO2 and LiNiO2 upon Li intercalation and de-intercalation, Phys. Chem. Chem. Phys. 11 (17) (2009) 3278–3289.
[58] A. Van der Ven, et al., First-principles investigation of phase stability in ${\mathrm {Li}}_{x}{\mathrm{CoO}}_{2}$, Phys. Rev. B 58 (6) (1998) 2975–2987.
[59] T. Li, et al., Degradation mechanisms and mitigation strategies of nickel-rich NMC-based lithium-ion batteries, Electrochemical Energy Reviews 3 (1) (2020) 43–80.
[60] A. Senyshyn, et al., Uniformity of flat Li-ion batteries studied by diffraction and imaging of X-rays and neutrons, ACS Appl. Energy Mater. 4 (4) (2021) 3110–3117.
[61] Y.-J. Gu, et al., Structural characterization of layered LiNi0.85 xMnxCo0.15O2 with x=0, 0.1, 0.2 and 0.4 oxide electrodes for Li batteries, J. Alloys Compd. 509 (30) (2011) 7915–7921.
[62] O. Sekizawa, et al., Crystal and electronic structure change determined by various method for delithiation process of Lix(Ni,Mn)O2-based cathode material, J. Power Sources 196 (16) (2011) 6651–6656.
[63] M. Ma, et al., Structural and electrochemical behavior of LiMn0.4Ni0.4Co0.2O2, J. Power Sources 165 (2) (2007) 517–534.
[64] Y. Makimura, et al., Microstructural observation of LiNi0.8Co0.15Al0.05O2after charge and discharge by scanning transmission electron microscopy, J. Electrochem. Soc. 159 (7) (2012) A1070–A1073.
[65] Z. Tang, et al., *Facilitating lithium-ion Diffusion in layered cathode Materials by introducing Li^{+}/Ni^{2+}Antisite Defects for high-rate Li-ion batteries*, Research 2019 (2019), 2198906.
[66] J. Zheng, et al., Role of superexchange interaction on tuning of Ni/Li disordering in layered Li(NixMnyCoz)O2, J. Phys. Chem. Lett. 8 (22) (2017) 5537–5542.
[67] H. Chen, J.A. Dawson, J.H. Harding, Effects of cationic substitution on structural defects in layered cathode materials LiNiO2, J. Mater. Chem.A 2 (21) (2014) 7988–7996.
[68] N.A. Chernova, et al., Layered LixNiyMnyCo1-2yO2 cathodes for lithium ion batteries: understanding local structure via magnetic properties, Chem. Mater. 19 (19) (2007) 4682–4693.
[69] P. Stephens, Phenomenological model of anisotropic peak broadening in powder diffraction, J. Appl. Crystallogr. 32 (2) (1999) 281–289.
[70] E. Estevez-Rams, et al., On the powder diffraction pattern of crystals with stacking faults, Phil. Mag. 83 (36) (2003) 4045–4057.
[71] M.M.J. Treacy, J.M. Newsam, M.W. Deem, A general recursion method for calculating diffracted intensities from crystals containing planar faults, Proc. Roy. Soc. Lond. Math. Phys. Sci. 433 (1889) 499–520, 1991.
[72] M. Leoni, A.F. Gualtieri, N. Roveri, Simultaneous refinement of structure and microstructure of layered materials, J. Appl. Crystallogr. 37 (1) (2004) 166–173.
[73] J.A. Nelder, R. Mead, A simplex method for function minimization, Comput. J. 7 (4) (1965) 308–313.
[74] S. Kirkpatrick, C.D. Gelatt Jr., M.P. Vecchi, Optimization by simulated annealing, Science 220 (4598) (1983) 671–680.
[75] C.G.E. Boender, et al., A stochastic method for global optimization, Math. Program. 22 (1) (1982) 125–140.
[76] M. Casas-Cabanas, J. Rodríguez-Carvajal, M.R. Palacín, FAULTS, a new program for refinement of powder diffraction patterns from layered structures, in: Ninth European Powder Diffraction Conference: Prague, September 2-5, 2004, Oldenbourg Wissenschaftsverlag, 2015, pp. 243–248.
[77] M. Casas-Cabanas, et al., FAULTS: a program for refinement of structures with extended defects, J. Appl. Crystallogr. 49 (6) (2016) 2259–2269.

[78] A.S. Menon, et al., Synthetic pathway determines the nonequilibrium crystallography of Li- and Mn-rich layered oxide cathode materials, ACS Appl. Energy Mater. 4 (2) (2021) 1924–1935.
[79] A.S. Menon, et al., Influence of synthesis routes on the crystallography, morphology, and electrochemistry of Li2MnO3, ACS Appl. Mater. Interfaces 12 (5) (2020) 5939–5950.
[80] A.S. Menon, et al., Synthesis–structure relationships in Li- and Mn-rich layered oxides: phase evolution, superstructure ordering and stacking faults, Dalton Trans. 51 (11) (2022) 4435–4446.
[81] C. Yin, et al., Boosting energy efficiency of Li-rich layered oxide cathodes by tuning oxygen redox kinetics and reversibility, Energy Storage Mater. 35 (2021) 388–399.
[82] M. Mock, et al., Atomistic understanding of the LiNiO2–NiO2 phase diagram from experimentally guided lattice models, J. Mater. Chem.A 9 (26) (2021) 14928–14940.
[83] B.M. May, et al., *Effect of synthetic Parameters on defects, structure, and electrochemical Properties of layered oxide* $LiNi_{0.80}Co_{0.15}Al_{0.05}O_2$, J. Electrochem. Soc. 165 (14) (2018) A3537–A3543.
[84] B. Mortemard de Boisse, et al., Coulombic self-ordering upon charging a large-capacity layered cathode material for rechargeable batteries, Nat. Commun. 10 (1) (2019) 2185.
[85] M. Reynaud, M. Casas-Cabanas, Order and disorder in NMC layered materials: a FAULTS simulation analysis, Powder Diffr. 32 (S1) (2017) S213–S220.
[86] S. Bette, et al., A routine for the determination of the microstructure of stacking-faulted nickel cobalt aluminium hydroxide precursors for lithium nickel cobalt aluminium oxide battery materials, J. Appl. Crystallogr. 53 (1) (2020) 76–87.
[87] B.B. Berkes, et al., On the gassing behavior of lithium-ion batteries with NCM523 cathodes, J. Solid State Electrochem. 20 (11) (2016) 2961–2967.
[88] G.-L. Xu, et al., Challenges and strategies to advance high-energy nickel-rich layered lithium transition metal oxide cathodes for Harsh operation, Adv. Funct. Mater. 30 (46) (2020), 2004748.
[89] S.-Y. Lee, et al., Revisiting primary particles in layered lithium transition-metal oxides and their impact on structural degradation, Adv. Sci. 6 (6) (2019), 1800843.
[90] Y. Bi, et al., Reversible planar gliding and microcracking in a single-crystalline Ni-rich cathode, Science 370 (6522) (2020) 1313–1317.
[91] S. Ahmed, et al., The role of intragranular nanopores in capacity fade of nickel-rich layered Li(Ni1–x–yCoxMny)O2 cathode materials, ACS Nano 13 (9) (2019) 10694–10704.
[92] P. Yan, et al., Intragranular cracking as a critical barrier for high-voltage usage of layer-structured cathode for lithium-ion batteries, Nat. Commun. 8 (1) (2017), 14101.
[93] A. Senyshyn, et al., Homogeneity of lithium distribution in cylinder-type Li-ion batteries, Sci. Rep. 5 (1) (2015), 18380.
[94] D. Petz, et al., Lithium distribution and transfer in high-power 18650-type Li-ion cells at multiple length scales, Energy Storage Mater. 41 (2021) 546–553.
[95] M.J. Mühlbauer, et al., Effect of fatigue/ageing on the lithium distribution in cylinder-type Li-ion batteries, J. Power Sources 348 (2017) 145–149.
[96] D. Petz, et al., Lithium heterogeneities in cylinder-type Li-ion batteries – fatigue induced by cycling, J. Power Sources 448 (2020), 227466.
[97] D.R. Sørensen, et al., Fatigue in high-energy commercial Li batteries while cycling at standard conditions: an in situ neutron powder diffraction study, ACS Appl. Energy Mater. 3 (7) (2020) 6611–6622.